Algebraic dynamic multilevel method for embedded discrete fracture model (F-ADM)

Mousa HosseiniMehr [a,b,*], Matteo Cusini [b], Cornelis Vuik [a], Hadi Hajibeygi [b]

[a] *Faculty of Electrical Engineering, Mathematics and Computer Science, Department of Applied Mathematics, Delft University of Technology, Van Mourik Broekmanweg 6, 2628 XE Delft, the Netherlands*
[b] *Faculty of Civil Engineering and Geosciences, Department of Geoscience and Engineering, Delft University of Technology, Stevinweg 1, 2628CV, Delft, the Netherlands*

ARTICLE INFO

ABSTRACT

We present an algebraic dynamic multilevel method for multiphase flow in heterogeneous fractured porous media (F-ADM), where fractures are resolved at fine scale with an embedded discrete modelling approach. This fine-scale discrete system employs independent fine-scale computational grids for heterogeneous matrix and discrete fractures, which results in linear system sizes out of the scope of the classical simulation approaches. To reduce the computational costs, yet provide accurate solutions, on this highly resolved fine-scale mesh, F-ADM imposes independent dynamic multilevel coarse grids for both matrix and lower-dimensional discrete fractures. The fully-implicit discrete system is then mapped into this adaptive dynamic multilevel resolution for all unknowns (i.e., pressure and phase saturation). The dynamic resolution aims for resolving sharp fronts for the transport unknowns, thus constant interpolators are used to map the saturation from coarse to fine grids both in matrix and fractures. However, due to the global nature of the pressure unknowns, local multilevel basis functions for both matrix and fractures with flexible matrix-fracture coupling treatment are introduced for the pressure. The assembly of the full sets of basis functions allows for mapping the solutions up and down between any resolutions. Due to its adaptive multilevel resolution, F-ADM develops an automatic integrated framework to homogenise or explicitly represent a fracture network at a coarser level by selection of the multilevel coarse nodes in each sub-domain. Various test cases, including multiphase flow in 2D and 3D media, are studied, where only a fraction of the fine-scale grids is employed to obtain accurate nonlinear multiphase solutions. F-ADM casts a promising approach for large-scale simulation of multiphase flow in fractured media.

© 2018 Elsevier Inc. All rights reserved.

1. Introduction

Many geo-engineering applications (e.g., hydrocarbon and geothermal energy production) are driven by underground fluid flow in large-scale ($O(10^3)$ [m]) heterogeneous fractured porous media [1]. Even at what is known as Darcy's

$(O(10^{-2})$ [m]) continuum scale, accurate and efficient simulation of flow through these formations remains challenging. This is because the simulation accuracy is often maintained with resolving the small scale heterogeneous rock properties, along with explicitly accounting for lower-dimensional fractures with highly contrasting properties compared with their hosting rock. On the other hand, the applicability of the simulation methods for real-field applications imposes a limiting bound on the amount of degrees of freedom that the linear systems can contain. Expectedly, this limitation becomes more pronounced in presence of fractures, and when multiphase flows with complex fluid and rock physics are considered. Therefore, there exist high demands for advanced methods which provide accurate and efficient (i.e., real-field applicable) simulations for flow in fractured subsurface formations.

Multiscale Finite-Element (MsFE) [2–4] and Finite-Volume (MsFV) [5–10] methods along with Dynamic Local Grid Refinement (DLGR) techniques [11–19] are two classes of such advanced methods that aim to achieve accurate and efficient simulations by tackling different aspects of the entire complexity map. Multiscale methods have been developed to efficiently solve the elliptic (or parabolic) pressure equation, which highly heterogeneous coefficients, by solving the system on a coarse grid while preserving the fine-scale heterogeneities. On the other hand, DLGR techniques adapt the grid resolution throughout the time-dependent simulation to employ a high-resolution grid where necessary (i.e., the advancing saturation front), and are, therefore, transport-oriented methods. The Algebraic Dynamic Multilevel (ADM) method [20] has been introduced to address the multi-scale multilevel coexistence of the pressure (elliptic or parabolic) and transport (hyperbolic) unknowns, at the same time, within both fully implicit (FIM) and sequential (implicit and explicit) simulation frameworks. ADM develops a dynamic multilevel system for all unknowns, through an algebraic formulation, where the resolutions are connected through sets of basis functions. ADM has been recently developed for multiphase flows in heterogeneous formations, with compositional and capillary effects [21].

ADM extends the applicability of the multiscale methods to fully-implicit (stable) simulations, allows for crossing the scales for all unknowns with a multilevel dynamic mesh, does not require reconstruction of conservative flux field, employs the basis functions which are computed only at the beginning of the simulation, and does not rely on any smoothing iterative procedure. The development of such a dynamic multilevel scheme for fractured media has not yet been addressed, despite their high importance in the geo-scientific community and extensive literature for fine-scale consistent discrete representations [22–32]. Such a dynamic multilevel approach allows for capturing explicit fractures at their relevant resolution while maintaining the scalability of the simulation for real-field applications.

In this work, an ADM method for simulation of multiphase flow in heterogeneous fractured porous media is developed (F-ADM). This is achieved by devising multilevel multiscale basis functions for embedded discrete fracture modelling (EDFM) approach [33–38]. More precisely, first, an EDFM fine-scale discrete system is obtained [39–41,34,42–45], which allows for independent grids for fractures and matrix. This makes it convenient to treat complex fracture geometries with multiple intersections [46,47]. Given this fine-scale discrete system, with fully implicit flow-transport coupling treatment, the F-ADM maps it to a dynamic multilevel nested resolution, both for the matrix and the fractures. Such a dynamic multilevel grid is obtained to employ fine-scale resolution only where needed (e.g., at the advancing saturation fronts).

Similar as in the fine-scale system, the ADM dynamic grid is chosen independently for matrix and fractures, based on a front-tracking criterion that aims to minimise the cost-accuracy trade-off. Mapping the solutions across different grid resolutions is performed through sequences of restriction and prolongation operators. Finite-volume restriction operators are employed for all unknowns to ensure mass conservation at all levels. On the other hand, different interpolation strategies are considered for the two main unknowns (pressure and saturation). Specifically, the devised multilevel multiscale basis functions are employed as pressure interpolators whereas piece-wise constant functions are used to interpolate saturation values, as the grid refinement strategy avoids crossing the scales at the saturation front locations.

Such a development allows for an automatic framework to explicitly or effectively represent a fracture at any coarse level, i.e., through the selection of the location of the coarse nodes. More precisely, if no coarse node for a fracture network inside a dual coarse grid is chosen, the matrix basis functions will automatically homogenise the effect of the fracture at the corresponding coarse scale. However, if coarse nodes are selected inside the fracture network of that dual coarse cell, the fractures will be explicitly represented at the corresponding coarser resolution. The accuracy and the sensitivity of the F-ADM to the error criterion and to the pressure basis functions are studied through a set of 2D and 3D test cases. The devised F-ADM strategy provides a dynamic treatment of highly fractured media, and casts a promising approach for real-field applications.

The rest of the paper is organised as follows. The governing equations, fine-scale discrete system and the simulation strategy are briefly presented in Section 2. Then, the F-ADM method for flow in porous media with embedded discrete fractures is described in Section 3. Numerical results are presented in Section 4. Finally, the paper is concluded in Section 5.

2. Fine-scale equations and solution strategy

2.1. Governing equations

Mass conservation for phase α in the absence of mass-exchange between phases, capillary, and gravitational effects, in porous media with n_{frac} discrete embedded fractures reads
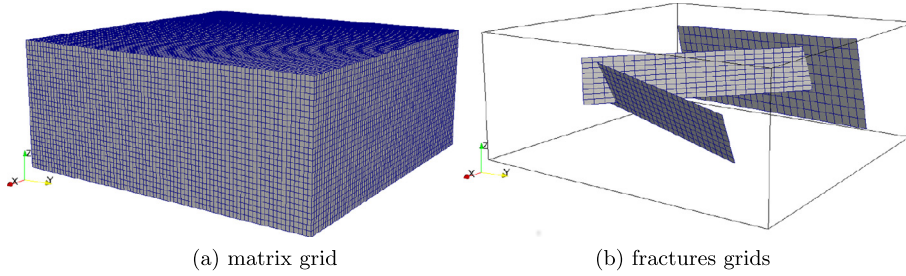
(a) matrix grid (b) fractures grids

Fig. 1. The independent matrix 3D grid and the fractures 2D grids are shown. Note that each domain has its own grid and that any fracture orientation can be considered.

$$\frac{\partial}{\partial t}\left(\phi^m \rho_\alpha^m S_\alpha^m\right) - \nabla \cdot \left(\rho_\alpha^m \boldsymbol{\lambda}^m \cdot \nabla p^m\right) = \sum_{i=1}^{n_{\text{frac}}} \rho_\alpha \mathcal{Q}_\alpha^{mf_i} + \rho_\alpha q_\alpha^m \quad \text{on} \quad \Omega_m \subseteq \Re^n \tag{1}$$

for the matrix and

$$\frac{\partial}{\partial t}\left(\phi^{f_i} \rho_\alpha^{f_i} S_\alpha^{f_i}\right) - \nabla \cdot \left(\rho_\alpha^{f_i} \boldsymbol{\lambda}^{f_i} \cdot \nabla p^{f_i}\right) =$$

$$\rho_\alpha \mathcal{Q}_\alpha^{f_i m} + \sum_{j=1}^{n_{\text{frac}}} \left(\rho_\alpha \mathcal{Q}_\alpha^{f_i f_j}\right)_{j \neq i} + \rho_\alpha q_\alpha^{f_i} \quad \text{on} \quad \Omega_{f_i} \subseteq \Re^{n-1} \quad \forall i \in \{1, ..., n_{\text{frac}}\} \tag{2}$$

for the lower-dimensional fractures. There exist n_α phases. Moreover, the superscripts m and f in Eqs. (1)–(2) indicate, respectively, the rock matrix and the fractures. Here, ϕ is the porosity of the medium, ρ_α, S_α, $\boldsymbol{\lambda}$ are, respectively, the density, saturation, and mobility of phase α. Moreover, $\boldsymbol{\lambda} = \frac{k_{r\alpha}}{\mu_\alpha}\mathbf{K}$ holds, where k_r, μ and $\mathbf{K}$ are phase relative permeability, viscosity and rock absolute permeability tensor, respectively. Also, q_α is the phase source term (i.e., wells). Finally, $\mathcal{Q}_\alpha^{mf_i}$ and $\mathcal{Q}_\alpha^{f_i m}$ are the phase flux exchanged between matrix and the i-th fracture, whereas $\mathcal{Q}_\alpha^{f_i f_j}$ represents the influx of phase α from j-th fracture to the i-th fracture. Note that mass balance enforces $\iiint_V \mathcal{Q}_\alpha^{mf_i} dV = -\iint_{A_{f_i}} \mathcal{Q}_\alpha^{f_i m} dA$ and $\iint_{A_{f_i}} \mathcal{Q}_\alpha^{f_i f_j} dA = -\iint_{A_{f_j}} \mathcal{Q}_\alpha^{f_j f_i} dA$.

Equations (1)–(2), subject to proper initial and boundary conditions, form a well-posed system for n_α unknowns, once the $\sum_{\alpha=1}^{n_\alpha} S_\alpha = 1$ constraint is employed to eliminate one of the phase saturation unknowns. Here, this system of equations is solved for two phase flow with primary unknowns of p and S_1 (from now on indicated as S).

2.2. Fine-scale discrete system

The coupled system of non-linear equations, i.e., Eqs. (1)–(2), is discretized in space with a two-point-flux-approximation (TPFA) finite-volume scheme in space and a backward (implicit) Euler scheme in time. Independent structured grids are generated for a three-dimensional (3D) porous medium and 2D fractures. An illustration is presented in Fig. 1. The advective TPFA flux between control volumes i and j reads

$$F_{\alpha,ij} = \rho_\alpha^* \frac{k_{r\alpha}^*}{\mu_\alpha^*} T_{ij}(p_i - p_j). \tag{3}$$

Here, $T_{ij} = \frac{A_{ij}}{d_{ij}} K_{ij}^H$ is the transmissibility between cells i and j. A_{ij} is the interface area between cells i and j, d_{ij} is the distance between the cells centres and K_{ij}^H is the harmonic average of the two permeabilities. The terms indicated with the superscript $*$ are evaluated using a phase potential upwind scheme. Following EDFM [34,46], the fluxes between a matrix cell i and a fracture cell j are modelled as

$$\mathcal{F}_{\alpha,ij}^{mf} = -\mathcal{F}_{\alpha,ij}^{fm} = -\rho_\alpha^* \frac{k_{r\alpha}^*}{\mu_\alpha^*} T_{ij}^{mf} (p_i^m - p_j^f), \tag{4}$$

where the transmissibility $T_{ij}^{mf} = K_{ij}^H CI_{ij}$. K_{ij}^H is the harmonic average permeability between the overlapping matrix and fracture elements, and CI_{ij} is the connectivity index between them. The EDFM models the matrix-fracture connectivity as $CI_{ij} = \frac{A_{ij}^{mf}}{\langle d \rangle_{ij}}$ where A_{ij}^{mf} is the area fraction of fracture cell j overlapping with matrix cell i (see Fig. 2), and $\langle d \rangle_{ij}$ is the average distance between these cells [34]. Note that the recently developed projection-based formulation (pEDFM) would lead to
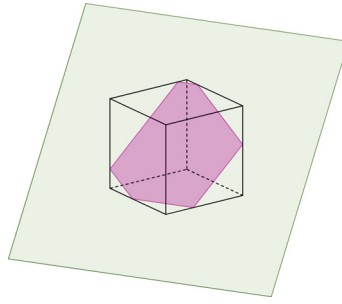
Fig. 2. Illustration of overlapping fracture and matrix cells, where the overlap section forms an irregular hexagon.
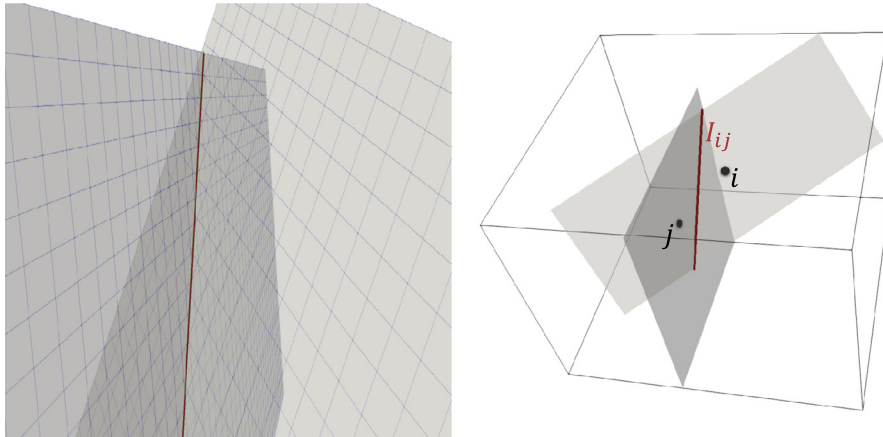

Fig. 3. Illustration of two intersecting fracture plates (left) and discrete elements (right), with the intersection lines shown in red. (For interpretation of the colours in the figure(s), the reader is referred to the web version of this article.)

a consistent embedded formulation [46], however, since we consider highly conductive fractures the difference between pEDMF and EDFM is minimal.

Similarly, the flux exchange between intersecting fracture elements i (belonging to fracture f) and j (belonging to fracture g) is modelled as

$$\mathcal{F}_{\alpha,ij}^{fg} = -\mathcal{F}_{\alpha,ij}^{gf} = -\rho_\alpha^* \frac{k_{r_\alpha}^*}{\mu_\alpha^*} T_{ij}^{fg} (p_i^f - p_j^g). \tag{5}$$

The transmissibility T_{ij}^{fg} between the two cells is computed based on a lower dimensional connectivity index formulation. The intersection of 2D fracture plates is a line, as shown in Fig. 3. Each two intersecting fracture cells intersect at a line segment I_{ij} (the red line in Fig. 3 (right)) with the average distances from the intersection segment of $\langle d \rangle_{i I_{ij}}^f \neq \langle d \rangle_{j I_{ij}}^g$. Therefore, T_{ij}^{fg} is calculated in a harmonic-average formulation as

$$T_{ij}^{fg} = K_{ij}^H \frac{CI_{i I_{ij}}^f \times CI_{j I_{ij}}^g}{CI_{i I_{ij}}^f + CI_{j I_{ij}}^g}, \tag{6}$$

where, e.g., $CI_{i I_{ij}}^f$ is the connectivity index between the 2D fracture element i and the 1D intersection segment I_{ij}. Thus, at each time-step the following system of equations is solved

$$\frac{(\phi^m \rho_\alpha^m S_\alpha^m)_i^{n+1} - (\phi^m \rho_\alpha^m S_\alpha^m)_i^n}{\Delta t} + \sum_{j=1}^{N_n} F_{\alpha,ij} + + \sum_{k=1}^{n_{\text{frac}}} \left(\sum_{j=1}^{N_{f_k}} \mathcal{F}_{\alpha,ij}^{mf_k} \right) = \rho_\alpha q_{\alpha,i}^m, \quad \forall i \in \{1, ..., N_m\} \tag{7}$$

in the matrix and

$$\frac{(\phi^{f_h} \rho_\alpha^{f_h} S_\alpha^{f_h})_i^{n+1} - (\phi^{f_h} \rho_\alpha^{f_h} S_\alpha^{f_h})_i^n}{\Delta t} + \sum_{j=1}^{N_n} F_{\alpha,ij} + \sum_{j=1}^{N_m} \mathcal{F}_{\alpha,ij}^{f_h m} +$$

$$+ \sum_{k=1}^{n_{\text{frac}}} \left(\sum_{j=1}^{N_{f_k}} \mathcal{F}_{\alpha,ij}^{f_h f_k} \right) = \rho_\alpha q_{\alpha,i}^{f_h}, \quad \forall i \in \{1, ..., N_{f_h}\}$$ (8)

in each fracture h. Here, N_m and N_{f_k} are the number of cells of the matrix and of fracture k. N_n indicates the number of neighbouring cells (2 in 1D, 4 in 2D, 6 in 3D). Equations (7)–(8) can be written in residual form as

$$(r_{\alpha,i}^m)^{n+1} = \rho_\alpha q_{\alpha,i}^m - \frac{(\phi^m \rho_\alpha^m S_\alpha^m)_i^{n+1} - (\phi^m \rho_\alpha^m S_\alpha^m)_i^n}{\Delta t} - \sum_{j=1}^{N_n} F_{\alpha,ij} - - \sum_{k=1}^{n_{\text{frac}}} \left(\sum_{j=1}^{N_{f_k}} \mathcal{F}_{\alpha,ij}^{m f_k} \right) \quad \forall i \in \{1, ..., N_m\}$$ (9)

for the rock matrix, and

$$(r_{\alpha,i}^{f_h})^{n+1} = \rho_\alpha q_{\alpha,i}^{f_h} - \frac{(\phi^{f_h} \rho_\alpha^{f_h} S_\alpha^{f_h})_i^{n+1} - (\phi^{f_h} \rho_\alpha^{f_h} S_\alpha^{f_h})_i^n}{\Delta t} - \sum_{j=1}^{N_n} F_{\alpha,ij} - \sum_{j=1}^{N_m} \mathcal{F}_{\alpha,ij}^{f_h m} -$$

$$- \sum_{k=1}^{n_{\text{frac}}} \left(\sum_{j=1}^{N_{f_k}} \mathcal{F}_{\alpha,ij}^{f_h f_k} \right), \quad \forall i \in \{1, ..., N_{f_h}\}$$ (10)

for fracture f_h. Let us define $r^n = [(r^m)^n, (r^{f_1})^n ... (r^{f_{n_{\text{frac}}}})^n]^T$ where $(r^k)^n$ is the residual vector of medium k at time-step n. Similarly, p^n and S^n indicate the vectors of pressure and saturation unknowns (of all media). The residual r^{n+1} is a non-linear function of the primary unknowns p^{n+1} and S^{n+1}. Thus, at each time-step a Newton–Raphson method is employed to solve the non-linear system iteratively, i.e.

$$r^{\nu+1} = r^\nu + \left. \frac{\partial r}{\partial p} \right|^\nu \delta p^{\nu+1} + \left. \frac{\partial r}{\partial S} \right|^\nu \delta S^{\nu+1} = 0$$ (11)

where the superscript ν is the iteration index. Consequently, at each Newton's iteration a linear-system $\mathbf{J}^\nu \delta x^{\nu+1} = -r^\nu$ is solved. Here, $\mathbf{J}^\nu$ is the Jacobian matrix with $\delta x^{\nu+1} = [\delta p, \delta S]^T$. Therefore, assuming two phases (w and o representing water and oil respectively), the linear system of equations can be written as

$$\underbrace{\begin{pmatrix} J_{op}^{mm} & J_{op}^{mf} & J_{os}^{mm} & J_{os}^{mf} \\ J_{op}^{fm} & J_{op}^{ff} & J_{os}^{fm} & J_{os}^{ff} \\ J_{wp}^{mm} & J_{wp}^{mf} & J_{ws}^{mm} & J_{ws}^{mf} \\ J_{wp}^{fm} & J_{wp}^{ff} & J_{ws}^{fm} & J_{ws}^{ff} \end{pmatrix}^\nu}_{\mathbf{J}_0^\nu} \underbrace{\begin{pmatrix} \delta p^m \\ \delta p^f \\ \delta S_w^m \\ \delta S_w^f \end{pmatrix}^{\nu+1}}_{\delta x_0^{\nu+1}} = - \underbrace{\begin{pmatrix} r_o^m \\ r_o^f \\ r_w^m \\ r_w^f \end{pmatrix}^\nu}_{r_0^\nu}$$ (12)

In this work, non-linear convergence is reached when the following conditions are satisfied:

$$||r||_\infty < \epsilon_1 \quad \wedge \quad \frac{||\delta p||_\infty}{||p||_\infty} < \epsilon_2 \quad \wedge \quad ||\delta S||_\infty < \epsilon_2.$$ (13)

Here, ϵ_1 and ϵ_2 are user-defined tolerances.

For real-field applications, as mentioned before, the solution of this nonlinear system of equations is challenging. Next, the F-ADM is presented as a promising framework for resolving this challenge.

3. F-ADM method

3.1. Solution strategy

At each Newton's iteration, F-ADM constructs an algebraically reduced system based on Eq. (12) on a multilevel grid which is dynamically defined at the beginning of each time-step. A schematic of F-ADM simulation is shown in Fig. 4.

As a first step, the F-ADM grid needs to be described. Sets of n_m and n_{f_i} nested Cartesian grids are imposed on the matrix and fracture fine-scale grid cells. The level at which the fine-scale computational domain is obtained is referred to as $l = 0$. Let N_m^l be the number of grid cells in the porous matrix and $N_{f_i}^l$ the number of grid cells in fracture i, both at level l. The coarsening ratio, γ^l can therefore be defined as

$$\gamma^l = \left(\gamma_m^l, \gamma_{f1}^l, \cdots, \gamma_{n_{\text{frac}}}^l \right) = \left(\frac{N_m^l}{N_m^{l-1}}, \frac{N_{f_1}^l}{N_{f_1}^{l-1}}, \cdots, \frac{N_{f_{n_{\text{frac}}}}^l}{N_{f_{n_{\text{frac}}}}^{l-1}} \right).$$ (14)
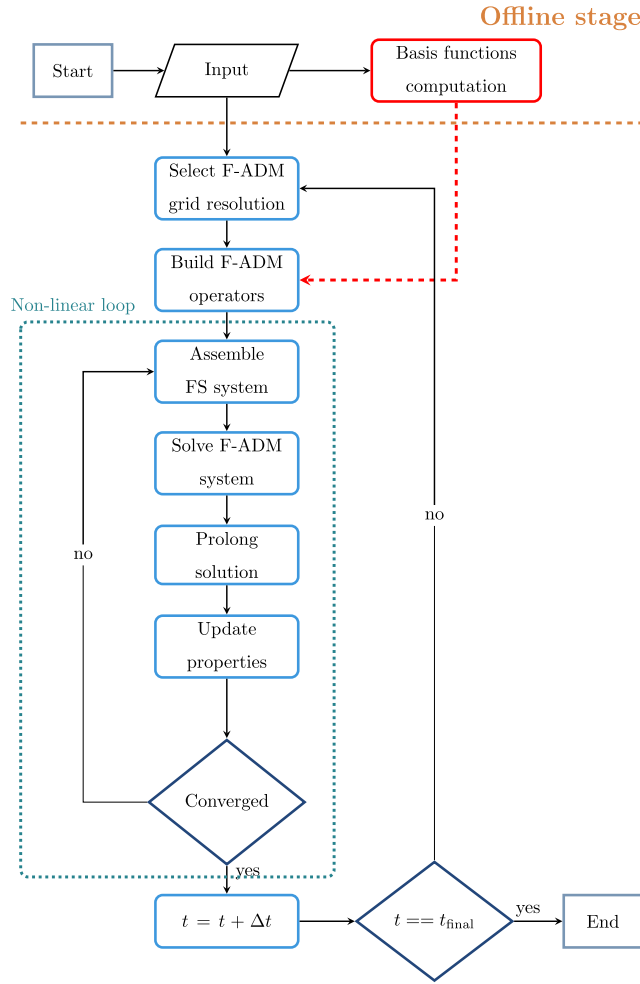
Fig. 4. Schematic description of F-ADM reservoir simulation.

Note that the count of coarsening levels and the coarsening ratios for the matrix and every individual fracture are independent, which leads to a flexible framework. Therefore, the F-ADM solution grid at each time-step is constructed by combining grid-cells at different resolutions.

F-ADM maps the fine-scale system to the dynamic multilevel grid by applying sequences of restriction ($\mathbf{R}$) and prolongation ($\mathbf{P}$) operators, which are constructed based on the values computed at the beginning of the simulation (Fig. 4). More precisely, at each iteration, the F-ADM system reads

$$\underbrace{\hat{\mathbf{R}}_l^{l-1} \dots \hat{\mathbf{R}}_1^0 \mathbf{Jo}\, \hat{\mathbf{P}}_0^1 \dots \hat{\mathbf{P}}_{l-1}^l}_{\mathbf{J}_{ADM}}\, \delta \hat{x}_l = - \underbrace{\hat{\mathbf{R}}_l^{l-1} \dots \hat{\mathbf{R}}_1^0 r_0}_{r_l}, \tag{15}$$

where $\hat{\mathbf{R}}_{l+1}^l$ is the restriction operator mapping part of the vector of solutions which are at resolution l ($\delta \hat{x}_l$) to resolution $l+1$ ($\delta \hat{x}_{l+1}$). Similarly, $\hat{\mathbf{P}}_l^{l+1}$ is the prolongation operator mapping part of the entire solution vector which are at level $l+1$ to level l. Once the F-ADM system is solved, the approximated solution at fine-scale resolution $\delta x_0'$ (reference fine-scale solution is represented as δx_0) is given by

$$\delta x_0 \approx \delta x_0' = \hat{\mathbf{P}}_0^1 \dots \hat{\mathbf{P}}_{l-1}^l\, \delta x_l. \tag{16}$$

The F-ADM prolongation operator $\mathbf{P}_{i-1}^i$ between every levels i and $i-1$ is obtained for the entire domain, though at each time step only a fraction of the domain needs to go through this map, which is illustrated by $\hat{\mathbf{P}}_{i-1}^i$ in Eq. (15). The prolongation operator $\mathbf{P}_{i-1}^i$ has a block structure which reads

$$\mathbf{P}_{i-1}^i = \begin{pmatrix} [(P_p)_{i-1}^i]_{mm} & [(P_p)_{i-1}^i]_{mf} & 0 & 0 \\ [(P_p)_{i-1}^i]_{fm} & [(P_p)_{i-1}^i]_{ff} & 0 & 0 \\ 0 & 0 & [(P_S)_{i-1}^i]_{mm} & 0 \\ 0 & 0 & 0 & [(P_S)_{i-1}^i]_{ff} \end{pmatrix}_{N_{i-1} \times N_i}. \tag{17}$$

Similarly, the restriction operator reads

$$\mathbf{R}_i^{i-1} = \begin{pmatrix} [R_i^{i-1}]_m & 0 & 0 & 0 \\ 0 & [R_i^{i-1}]_f & 0 & 0 \\ 0 & 0 & [R_i^{i-1}]_m & 0 \\ 0 & 0 & 0 & [R_i^{i-1}]_f \end{pmatrix}_{N_i \times N_{i-1}}. \tag{18}$$

A finite-volume restriction operator is employed in order to guarantee mass conservation as convergence is reached on the multilevel F-ADM grid, i.e.,

$$R_i^{i-1}(s,t) = \begin{cases} 1 & \text{if cell } s \text{ is inside coarser cell } t, \\ 0 & \text{otherwise.} \end{cases} \tag{19}$$

On the other hand, the pressure and saturation blocks of the prolongation operator, $(P_p)_{i-1}^i$ and $(P_S)_{i-1}^i$ are different [20] as different interpolation rules are used for each variable. In this work $(P_S)_{i-1}^i = R_i^{i-1}{}^T$, where the superscript T indicates the transpose operator. The $(P_p)_{i-1}^i$ blocks, instead, are constructed following a multilevel multiscale procedure for fractured media developed in this work and described in the next subsection.

3.2. Fracture multilevel multiscale basis functions

The sub-block $(P_p)_{i-1}^i$ in the prolongation operator interpolates the pressure from resolution i to $i-1$. Here, the two-level multiscale strategy [36] is extended to multiple levels. Even though the fine-scale pressure equation is a TPFA-based system, starting from coarse level 1, all the coarse-scale systems develop MPFA-based connectivities, due to the local basis functions. Here, the MPFA-based pressure matrix A_p^{i-1}, which stands as fine-scale system for level $i-1$, is constructed by the multiscale finite-element procedure as

$$\tilde{A}_p^{i-1} = (\mathbf{P}_{i-2}^{i-1})^T A_p^{i-2} \mathbf{P}_{i-2}^{i-1}. \tag{20}$$

Then, $\tilde{A}_p^{i-1}$ is reduced to a TPFA-based system, i.e.,

$$A_p^{i-1} = tpfa(\tilde{A}_p^{i-1}), \tag{21}$$

where the $tpfa(\bullet)$ extracts the TPFA components of the matrix (heptadiagonal matrix for 3D Cartesian grids), by considering the transmissibility between cells i and j equal to entry A_{ij} of the original matrix. The algebraic multiscale procedure for the calculation of basis functions is now performed on this TPFA system at level $i-1$ [36], in order to obtain the basis functions at level i, i.e., $(P_p)_{i-1}^i$. Note that the TPFA reduction of the MPFA multilevel system is done independently for each sub-domain of matrix, and individual fractures.

In addition, similar as for the two-level multiscale strategy [36], F-ADM allows for full flexibility in the choice of the coupling strategy at all multilevel resolutions. In general, the pressure prolongation operator of a given level i reads

$$(P_p)_{i-1}^i = \left[(P_p^m)_{i-1}^i \quad (P_p^f)_{i-1}^i \right] = \begin{bmatrix} (P_p^{mm})_{i-1}^i & (P_p^{mf})_{i-1}^i \\ (P_p^{fm})_{i-1}^i & (P_p^{ff})_{i-1}^i \end{bmatrix}. \tag{22}$$

Here, the blocks $(P_p^m)_{i-1}^i$ and $(P_p^f)_{i-1}^i$ contain the basis functions corresponding to the matrix and fracture coarse-scale unknowns. Each one, e.g., $(P_p^m)_{i-1}^i$, can have nonzero values inside matrix and fracture sub-domains, depending on the local coupling strategy. More precisely, while the fully-coupled approach leads to nonzero sub-blocks of $(P_p^{mf})_{i-1}^i$ and $(P_p^{fm})_{i-1}^i$, the decoupled approach would lead to zero values in these local coupling sub-blocks. Fig. 5 shows a surface plot of some matrix and fracture basis functions at two different coarsening levels for a 2D homogeneous domain. A detailed description of the two-level basis function entries can be found in [36].
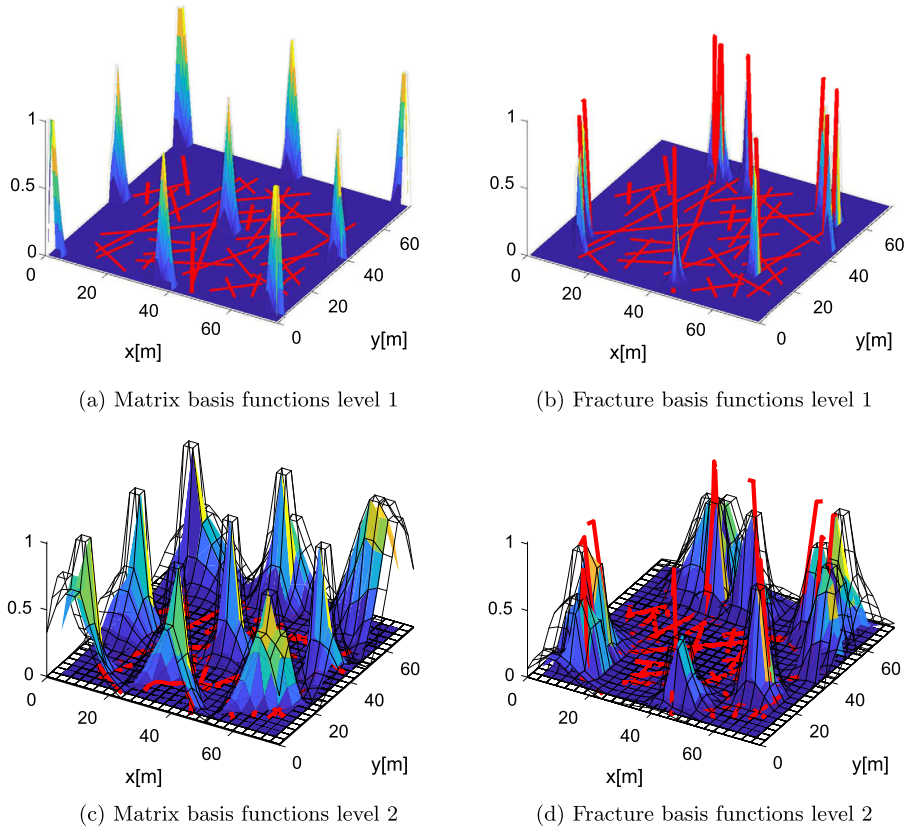
(a) Matrix basis functions level 1

(b) Fracture basis functions level 1

(c) Matrix basis functions level 2

(d) Fracture basis functions level 2

Fig. 5. Example of multilevel coupled basis functions for a 2D homogeneous domain. Matrix (left column) and fracture (right column) basis functions for coarsening levels 1 (top row) and 2 (bottom row) are shown.

3.3. Selection of the grid resolution

At each time-step, the F-ADM solution grid is constructed by combining grid cells of the previously defined sets of grids both in the matrix and in the fractures. The grid resolution at time-step $n+1$ is chosen based on the saturation map at time-step n, thus employing an explicit procedure. A semi-implicit gridding strategy [48] could also be used to avoid misplacement of the grid. Fig. 6 shows an example of a 3D test case with one fracture plate, for simplicity of the illustration. Two coarse levels are employed in the matrix along with one coarse level in the fracture. The grid selection method is applied independently in the matrix and in the fractures, therefore, different criteria can be set for each medium.

Since no well-functions are employed in dynamic simulations, fine-scale resolution is kept around all wells at all time.

4. Numerical results

Numerical results are presented in this section. First, the EDFM model for two-phase flow is validated, then the accuracy of a multilevel multiscale method for single phase flow on homogeneous and heterogeneous test cases is assessed. Finally, the accuracy and sensitivity of the proposed F-ADM method are investigated for both 2D and 3D domains. F-ADM results are compared against fine-scale simulations, used as a reference.

In all test cases, fluids and rocks are considered to be incompressible and quadratic relative permeability functions are used.

4.1. Test Case 1: validation of EDFM

To validate the EDFM implementation, a 2D homogeneous reservoir of $9\,\text{m} \times 9\,\text{m}$ is considered as shown in Fig. 7. A cross-shaped fracture network is present in the middle of the domain. Each fracture segment is 5 [m] long, with a permeability value of 10^9 times higher than that of the rock matrix ($K_m = 2.5 \cdot 10^{-13}\,\text{m}^2$ and $K_f = 1.3 \cdot 10^{-4}\,\text{m}^2$). The fracture aperture is $4 \cdot 10^{-2}$ m. Two incompressible fluid phases are considered. The reservoir has an initial saturation $S_{1,init} = 0.1$. No flow boundary conditions are considered at the top and bottom boundaries whereas the left and right boundaries have fixed pressures of $2.0 \cdot 10^7$ Pa and $1.0 \cdot 10^7$ Pa, respectively. Phase 1 is injected from the left boundary whereas production occurs at the right.
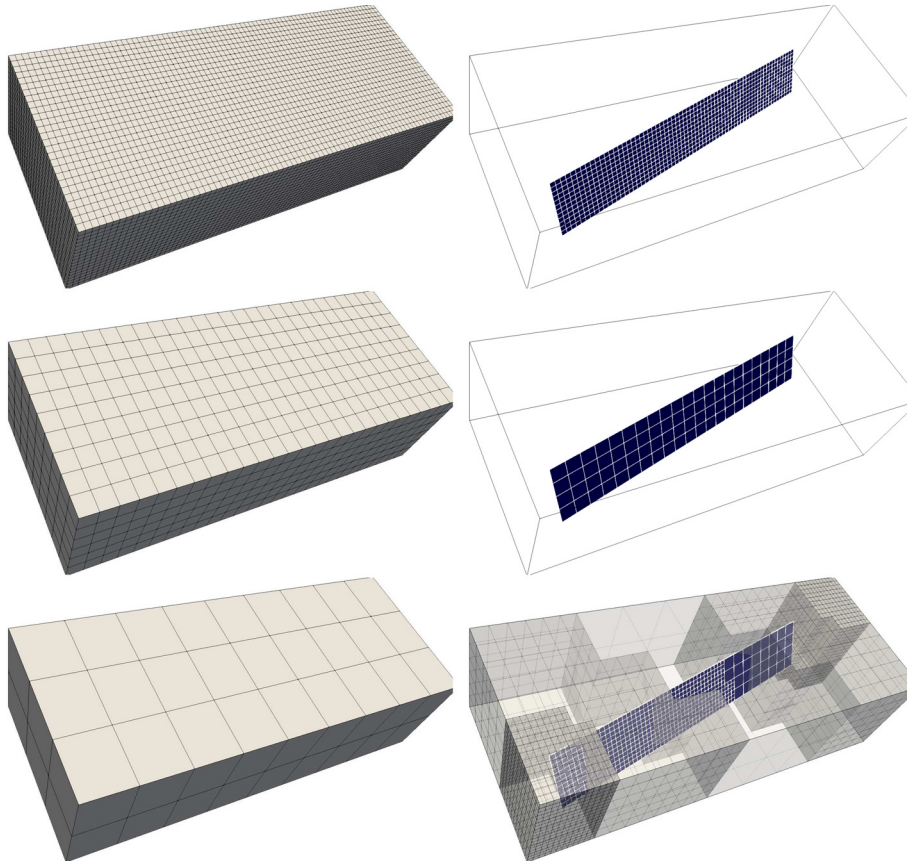
Fig. 6. Example of F-ADM grid selection for a 3D test case with one single planar fracture. Two coarse levels are used in matrix ($l = 1, 2$) and one coarse level is used in the fracture ($l = 1$). The bottom right figure shows an example of a dynamic grid.
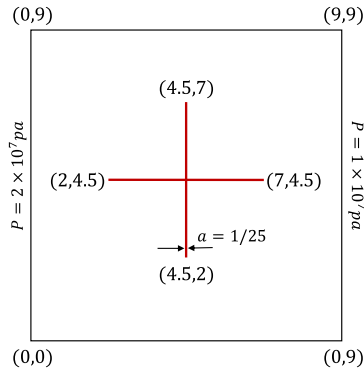

Fig. 7. Visualization of the 2D domain with a cross-shaped fracture network at the center.

The reference solution (referred to as DNS) is obtained by imposing a 225×225 grid that allows to fully resolve the flow inside the fracture. EDFM simulations are performed with three different matrix grid resolutions of 15×15, 25×25, and 45×45. The grid-cells inside the fractures are chosen to have similar dimensions as the matrix cells. The time-step size is 10^{-4} day for all simulations. The pressure and saturation maps after 0.0235 [Days] are shown in Fig. 8. Note that errors decreases upon refinement of the EDFM solution grid.

Figs. 9a and 9b present the pressure and saturation errors as functions of the simulation time. Given a variable x (i.e., pressure or saturation), the error, e_x, is calculated as

$$e_x = \frac{||x_{\text{DNS}} - x_{\text{EDFM}}||_2}{||x_{\text{DNS}}||_2}. \tag{23}$$
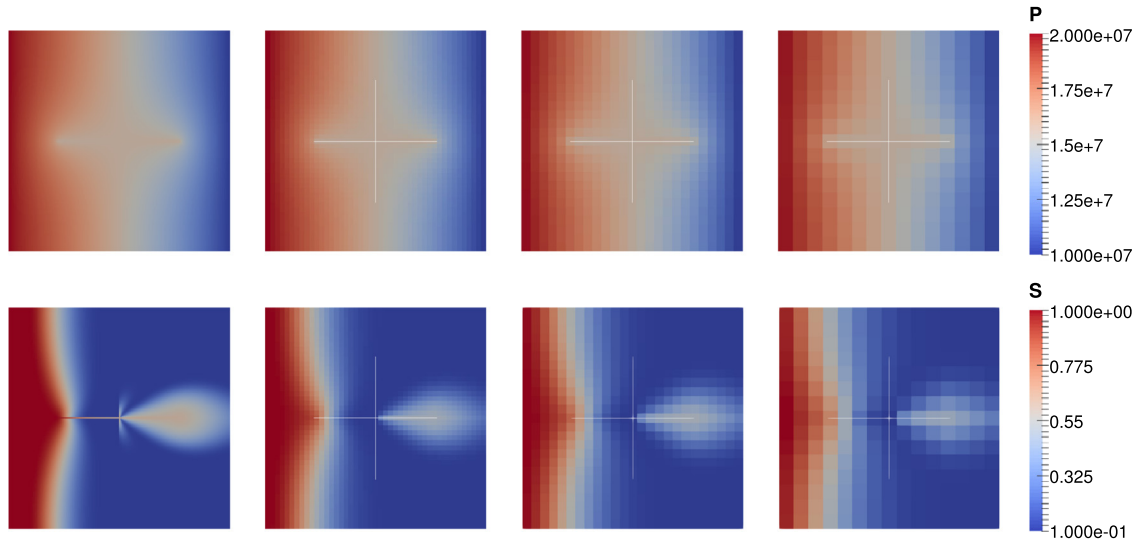
Fig. 8. Comparison of the fully resolved DNS (left column) using 225×225 cells and EDFM results with different grid resolutions (left to right: 45×45, 25×25, 15×15) after 0.0235 [Days]. Pressure is shown on the top, while the saturation map is illustrated in the bottom.
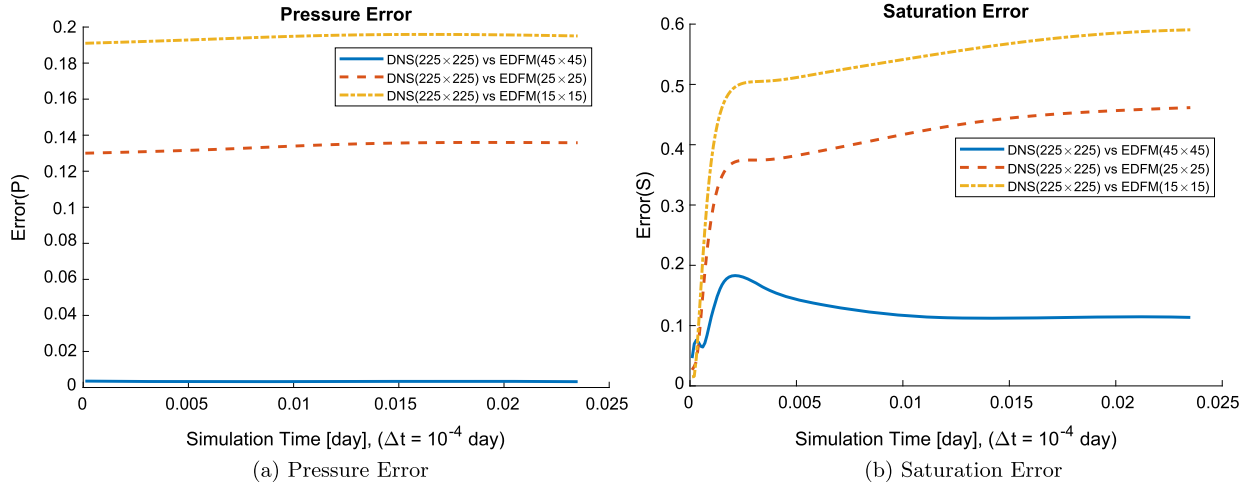

(a) Pressure Error

(b) Saturation Error

Fig. 9. Pressure and saturation errors of EDFM simulations with respect to the reference solution (DNS).

4.2. Test Case 2: F-ADM for single-phase flow in a 2D homogeneous fractured reservoir

Here, the accuracy of the F-ADM method for incompressible single-phase flow in fractured porous media is assessed. In this case, no grid adaptivity is employed and F-ADM is equivalent to a multilevel multiscale method. Thus, the objective of this test case is to verify the proposed multilevel interpolation strategy. A 2D fractured $75\,\text{m} \times 75\,\text{m}$ reservoir with 35 fractures is considered. A 375×375 grid is imposed on the rock matrix. Fractures have different lengths but identical apertures of $5 \cdot 10^{-3}\,\text{m}$. The fracture network consists of 4420 grid cells (for a total 145045 cells). The matrix permeability is $10^{-14}\,\text{m}^2$ whereas fractures permeability is $2.08 \cdot 10^{-6}\,\text{m}^2$. Two injection wells in bottom left and top left corners ($p_{\text{inj}} = 2 \cdot 10^7\,\text{Pa}$) and two production wells in bottom right and top right corners ($p_{\text{prod}} = 1 \cdot 10^7\,\text{Pa}$) are present.

The multilevel multiscale method is run with different number of coarse levels and coarsening ratios. Here, fully-coupled multiscale basis functions are considered. The error of the multiscale pressure solution (p_{ms}) with respect to the fine-scale pressure map (p_{fs}) is calculated as

$$e_p = \frac{||p_{\text{fs}} - p_{\text{ms}}||_2}{||p_{\text{fs}}||_2}. \tag{24}$$

The settings of each multiscale run, the pressure error (e_p) and the number of degrees of freedom are presented in Table 1. Remark that the error is larger when a higher number of levels or larger coarsening ratios are employed. However, the order of magnitude of the multiscale error is the same for all multilevel multiscale settings. Moreover, the coarsening levels in

Table 1
Settings and errors of the multilevel multiscale runs.

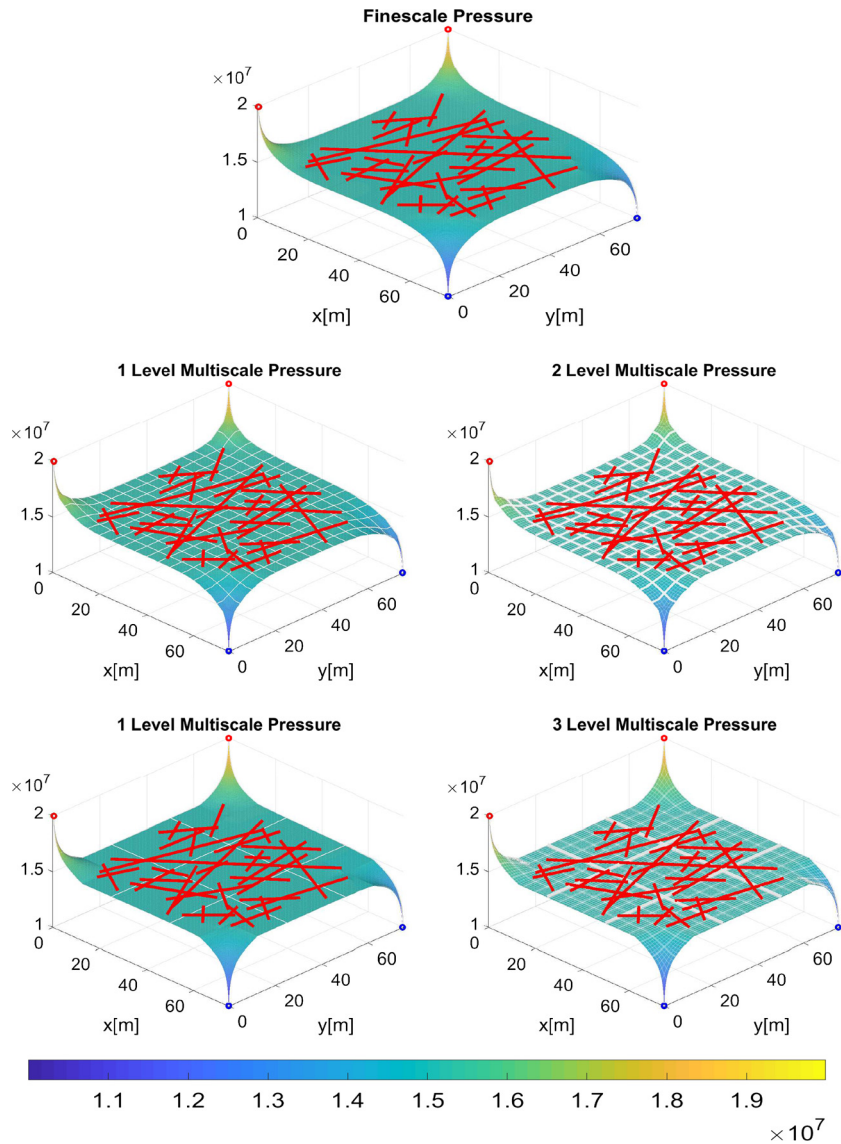|	Num. coarse levels	γ_m	Total DOF	e_p [%]
Case 1	1	5×5	6509	0.11
Case 2	1	25×25	1109	0.22
Case 3	2	5×5	877	0.27
Case 4	1	125×125	893	0.64
Case 5	3	5×5	661	0.98

Fig. 10. Test case 2 – comparison of the pressure distribution obtained by fine-scale simulations and F-ADM single-phase solver with enforced static multilevel multiscale, where the pressure is solved everywhere at the coarsest level. Top plot is the fine-scale solution. Middle row shows 1 level multiscale solution with $\gamma_m = 25 \times 25$ (left) and 2 level multiscale solution with $\gamma_m = 5 \times 5$ (right). Shown in the bottom row is 1 level multiscale solution with $\gamma_m = 125 \times 125$ (left) and 3 level multiscale solution with $\gamma_m = 5 \times 5$ (right). Note that the error norm are presented in Table 1.

matrix and fractures are independent of each other. Therefore, the maximum coarsening level in each domain (i.e., matrix and every individual fracture) can be different depending on its size and its number of grid cells.

The surface plots of the pressure distributions obtained with fine-scale simulations and with different multilevel multiscale settings are presented in Fig. 10.
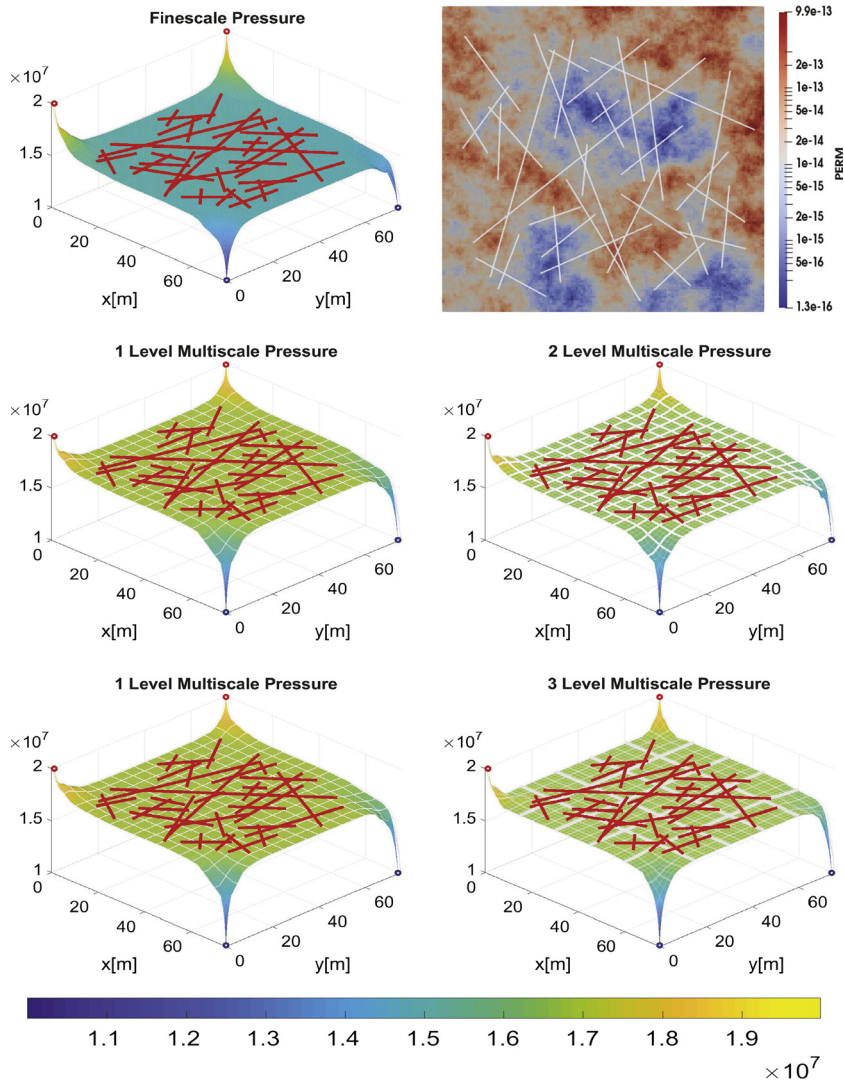
Fig. 11. Test case 3 – comparison of the pressure distribution obtained by fine-scale simulations and F-ADM single-phase solver with enforced static multilevel multiscale on heterogeneous domain, where the pressure is solved everywhere at the coarsest level. Shown on the top row are the permeability map (right) and the fine-scale solution (left). Middle row shows 1-level multiscale solution with $\gamma_m = 9 \times 9$ (left) and 2 level multiscale solution with $\gamma_m = 3 \times 3$ (right). Bottom row includes 1 level multiscale solution with $\gamma_m = 27 \times 27$ (left) and 3 level multiscale solution with $\gamma_m = 3 \times 3$ (right). Note that the error norm are presented in Table 2.

4.3. Test Case 3: F-ADM for single-phase flow in a 2D heterogeneous fractured reservoir

A heterogeneous 2D domain of 75 m × 75 m with a network of 35 fractures is considered. The matrix and fracture grids are 135 × 135 and 1665, respectively, resulting in 19890 total grid cells. The top right plot on Fig. 11 shows the heterogeneous permeability map for this test case with the minimum and maximum values of $1.3 \times 10^{-16}\,\mathrm{m}^2$ and $9.9 \times 10^{-13}\,\mathrm{m}^2$, respectively. Wells are located and have the same constraints as in the previous test case. Different coarsening levels and ratios are considered.

The pressure error with respect to the reference (i.e., fine-scale solution) is calculated based on Eq. (24), which is shown in Table 2 for different numbers of degrees of freedom (DOF). All multiscale runs employ fully-coupled basis functions. As it can be seen in Table 2, for the corresponding coarsening ratios, the multilevel multiscale and the 1-level multiscale strategies deliver comparable results. Note that no iterations have been employed to improve the multiscale results [36].

### 4.4. Test Case 4: multi-phase flow in a 2D homogeneous fractured reservoir

The same fractured homogeneous reservoir presented in the previous test case is considered. The rock matrix is discretized with a 135 × 135 fine-scale grid and 1665 grid cells are employed for the fractures (total domain grid

Table 2
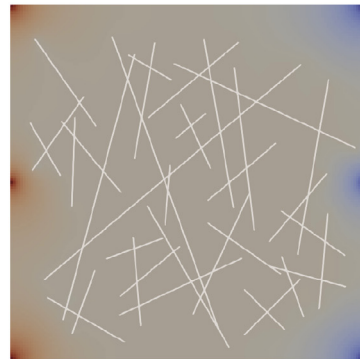Settings and errors of the multilevel multiscale runs for heterogeneous test case.

	Num. coarse levels	γ_m	Total DOF	e_p [%]
Case 1	1	3×3	2580	12.8
Case 2	1	9×9	780	12.7
Case 3	2	3×3	410	13.6
Case 4	1	27×27	580	11.0
Case 5	3	3×3	210	12.1
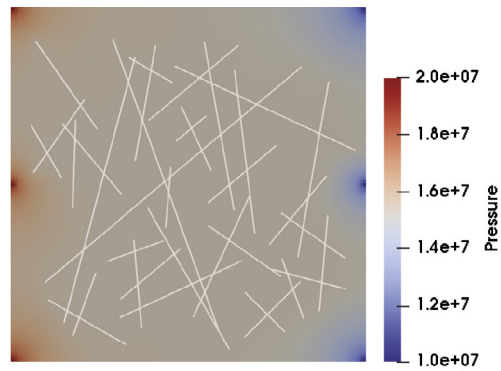
(a) Fine-scale
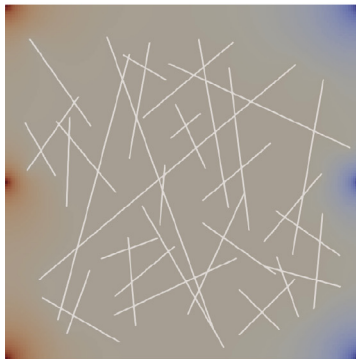
(b) error= 1.88×10^{-4}

(c) error= 3.25×10^{-3}
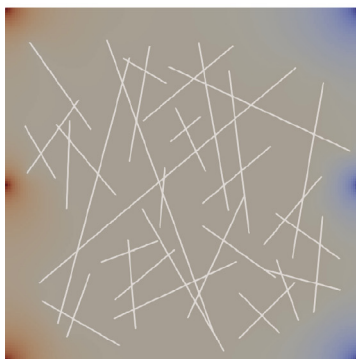
(d) error= 3.49×10^{-4}

(e) error= 2.28×10^{-3}

Fig. 12. Pressure plots for 2D F-ADM test case. Shown are the fine-scale solution (a), decoupled F-ADM with thresholds 0.1 (b) and 0.8 (c), and coupled F-ADM with thresholds 0.1 (d) and 0.8 (e), respectively.
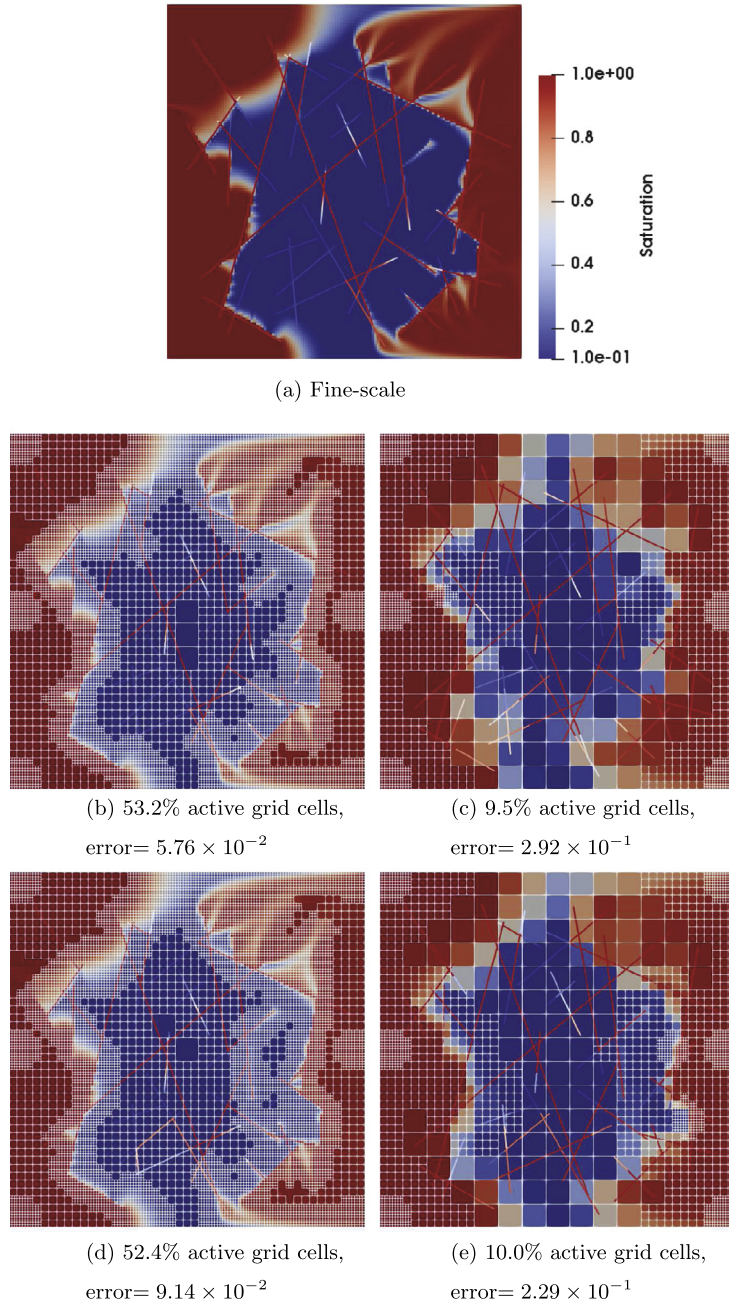
(a) Fine-scale

(b) 53.2% active grid cells,

error= 5.76×10^{-2}

(c) 9.5% active grid cells,

error= 2.92×10^{-1}

(d) 52.4% active grid cells,

error= 9.14×10^{-2}

(e) 10.0% active grid cells,

error= 2.29×10^{-1}

Fig. 13. Saturation distribution of fine-scale (a), decoupled F-ADM with thresholds 0.1 (b) and 0.8 (c), and coupled F-ADM with thresholds 0.1 (d) and 0.8 (e), respectively.

cells: 19890). F-ADM employs 2 coarse levels with coarsening ratio of 3 in each direction both for the matrix and the fractures. Both decoupled and fully-coupled multiscale basis functions are considered as pressure interpolators. The saturation difference between neighbouring cells is used as the F-ADM coarsening criterion with four different threshold values: $\Delta S = \{0.1, 0.3, 0.5, 0.8\}$. Three equidistant injection wells ($p_{\text{inj}} = 2 \cdot 10^7 \, \text{Pa}$) and three equidistant production wells ($p_{\text{prod}} = 1 \cdot 10^7 \, \text{Pa}$) are present at the left and right boundaries, respectively. The total simulation time is set to 1000 days.

Figs. 12 and 13 show the pressure and the saturation maps at the end of the simulation for fine-scale and F-ADM with 2 different threshold values for the coarsening criterion.
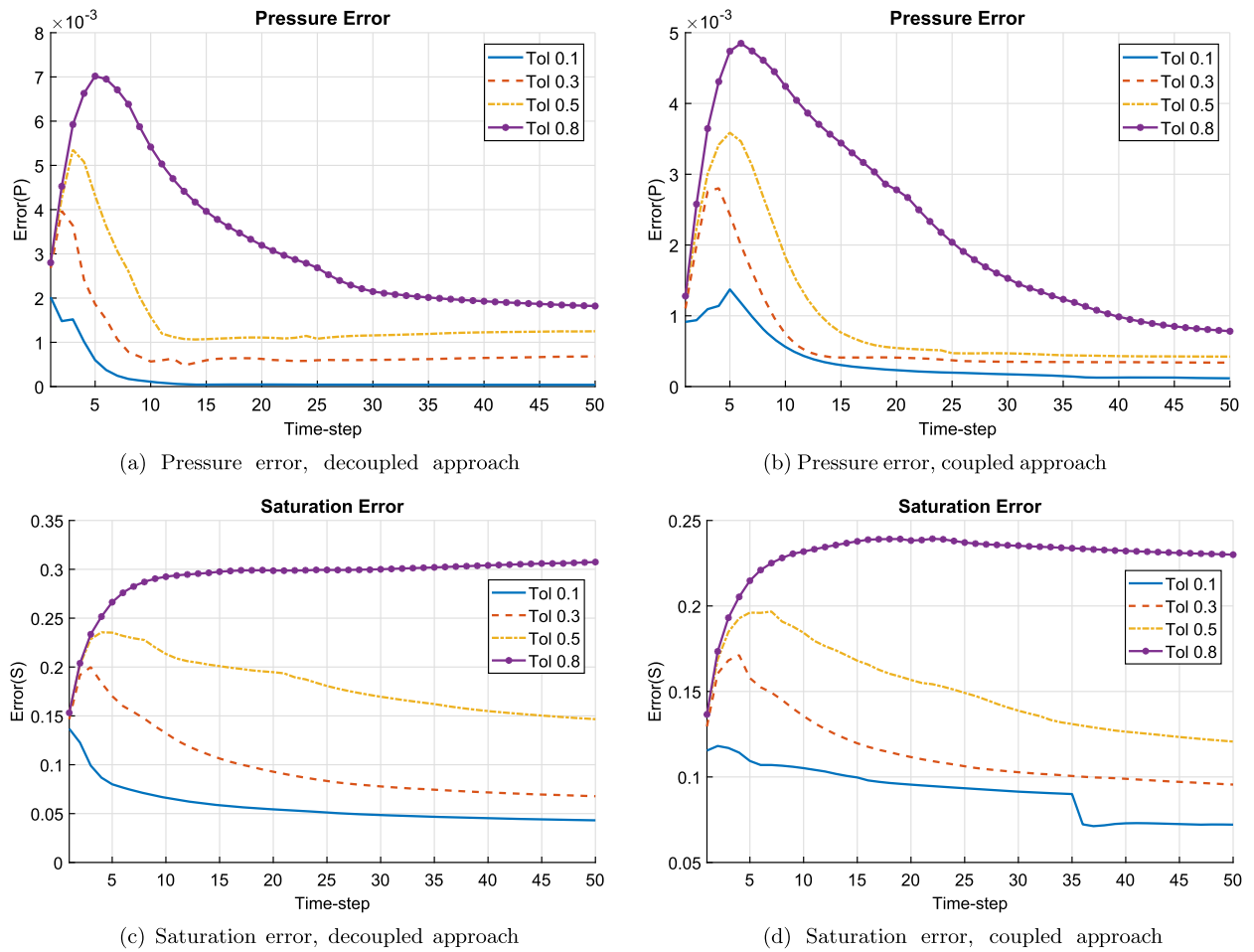
Fig. 14. Pressure and saturation errors: Fig. 14a and Fig. 14b show F-ADM error of pressure over simulation time-steps for decoupled and coupled basis functions approaches. Figs. 14c and 14d are plots of saturation error over simulation time-steps for decoupled and coupled approach respectively. The errors are calculated based on Eq. (25).

The error for pressure and saturation is calculated as

$$e_x = \frac{||x_{\mathrm{ms}} - x_{\mathrm{fs}}||_2}{||x_{\mathrm{fs}}||_2} \tag{25}$$

where, x is either pressure or saturation and the subscripts ms and fs indicate multiscale and fine-scale, respectively.

Figs. 14a, 14b and 14c, 14d show the F-ADM (both using decoupled and coupled basis functions) pressure and saturation errors at each time-step for the four values of the coarsening criterion. Figs. 15a and 15b illustrate the amount of active grid cells (as a percentage of the fine-scale number of cells) for each time-steps. Note that grid cells around wells are always kept at the fine-scale resolution. Here, 864 grid cells are kept at fine-scale resolution due to near-well refinement, which is 4.74 percent out of the 8.61 percent of active grid cells at the first time-step. Figs. 15c and 15d provide the average pressure and saturation errors along with the average percentage of grid cells employed by F-ADM as functions of the coarsening criterion threshold value.

F-ADM results show a low sensitivity to the type of basis functions employed. Note that coupled basis functions are more computationally expensive and provide with a denser prolongation operator. However, in case of using static prolongation operators, as basis functions of all levels are computed only once at the beginning of simulation, the extra computational costs involved in calculation of coupled basis functions can be considered negligible.

4.5. Test Case 5: multi-phase flow in a 2D heterogeneous fractured reservoir

This test case differs from test case 4 only in permeability of matrix as it is heterogeneous. The rest of the input parameters and configurations are identical to Test Case 4. The permeability map is identical to one used in test case 3, with heterogeneity contrast of 7.7×10^3. The well positioning follows the same configuration (line drive with 3 equidistant injectors and producers). Moreover, coarsening level, coarsening ratio and coarsening criteria are the same. As for their
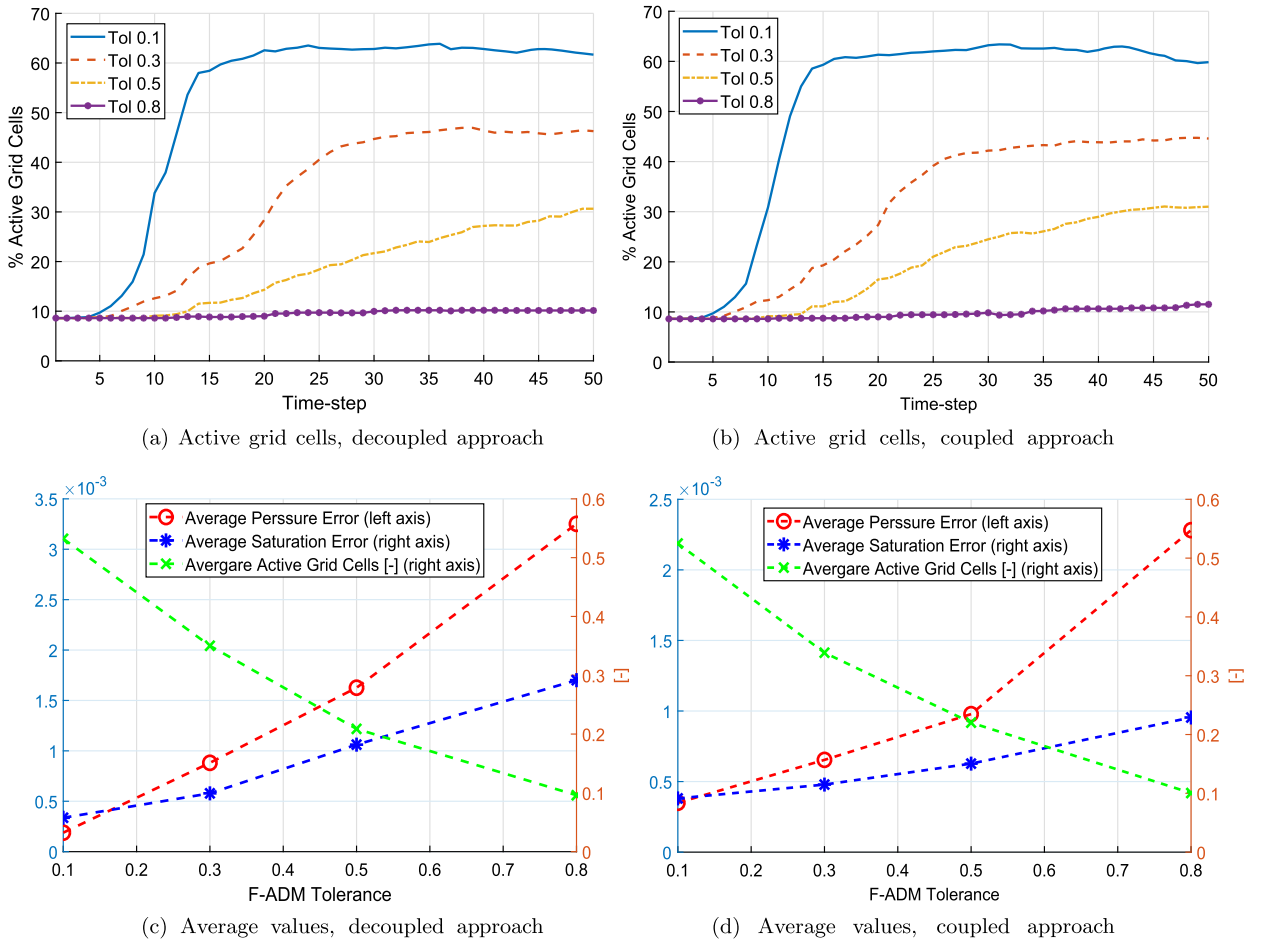
(a) Active grid cells, decoupled approach

(b) Active grid cells, coupled approach

(c) Average values, decoupled approach

(d) Average values, coupled approach

Fig. 15. Active grid cells and averaged parameters: Fig. 15a and Fig. 15b demonstrate the percentage of active grid cells for the two mentioned approaches respectively. The data is obtained over simulation time-steps and for four different F-ADM tolerances. Figs. 15c and 15d show the average of pressure error, saturation error and percentage of active grid cells over the whole simulation time for both approaches.

similar performance to decoupled approach, only the results of fully coupled basis functions are presented for pressure and saturation, in Figs. 16 and 17, respectively.

The F-ADM error is calculated using the same formulation as in the previous test cases, i.e. Eq. (25), and presented in Figs. 18a and 18b, respectively, for pressure and saturation. In addition, Fig. 18c shows the amount of active grid cells during the simulation for different coarsening tolerence values. Finally, Fig. 18d provides the average pressure and saturation errors along with the average percentage of grid cells as functions of the coarsening threshold value.

4.6. Test Case 6: multi-phase flow in a 3D homogeneous fractured reservoir

A 3D $75\,\mathrm{m} \times 75\,\mathrm{m} \times 30\,\mathrm{m}$ containing 26 fracture plates of different geometrical properties as shown in Fig. 19. The matrix is discretized with a $99 \times 99 \times 27$ Cartesian grid for a total of $264,627$ cells. Independent 2D grids are imposed on each fracture plate. The grid cells in the fractures have sizes $\Delta\xi$ and $\Delta\eta$ such that $mean(\Delta\xi, \Delta\eta) = 2 \times mean(\Delta x_m, \Delta y_m, \Delta z_m)$. Here, $\Delta x_m, \Delta y_m, \Delta z_m$ indicate the sizes of the matrix grid cells in each direction. The total number of grid cells in the fracture network is $2,646$ grid cells. The rock matrix permeability is $10^{-14}\,\mathrm{m}^2$ whereas the fractures one is $2.08 \cdot 10^{-6}\,\mathrm{m}^2$. Three injection wells are present in the bottom left, middle left and top left boundary, all perforating through the whole thickness of the reservoir ($p_{\mathrm{inj}} = 2 \cdot 10^7$ Pa). Similarly three production wells are located on the right-hand side of the domain ($p_{\mathrm{prod}} = 1 \cdot 10^7$ Pa). The simulation time is 1000 days.

F-ADM employs 2 levels of coarsening with coarsening ratios equal to 3 in each direction. Fig. 20 shows, for example, the saturation distribution at time-step 15 along with the F-ADM grid employed at that time-step. The same error measures used for the previous test case are considered. Figs. 21a and 21b present pressure and saturation errors at each time-step for four different threshold values of the coarsening criterion, i.e. 0.1, 0.3, 0.5 and 0.8. The evolution of the number of active grid cells throughout F-ADM simulations is shown in Fig. 21c. Average pressure error, saturation error and active grid cells over the whole simulation time versus ΔS thresholds are given in Fig. 21d. In this test case, 23328 grid cells

(a) Fine-scale

(b) error= 5.30×10^{-5}　　　　　　　(c) erorr= 1.96×10^{-4}

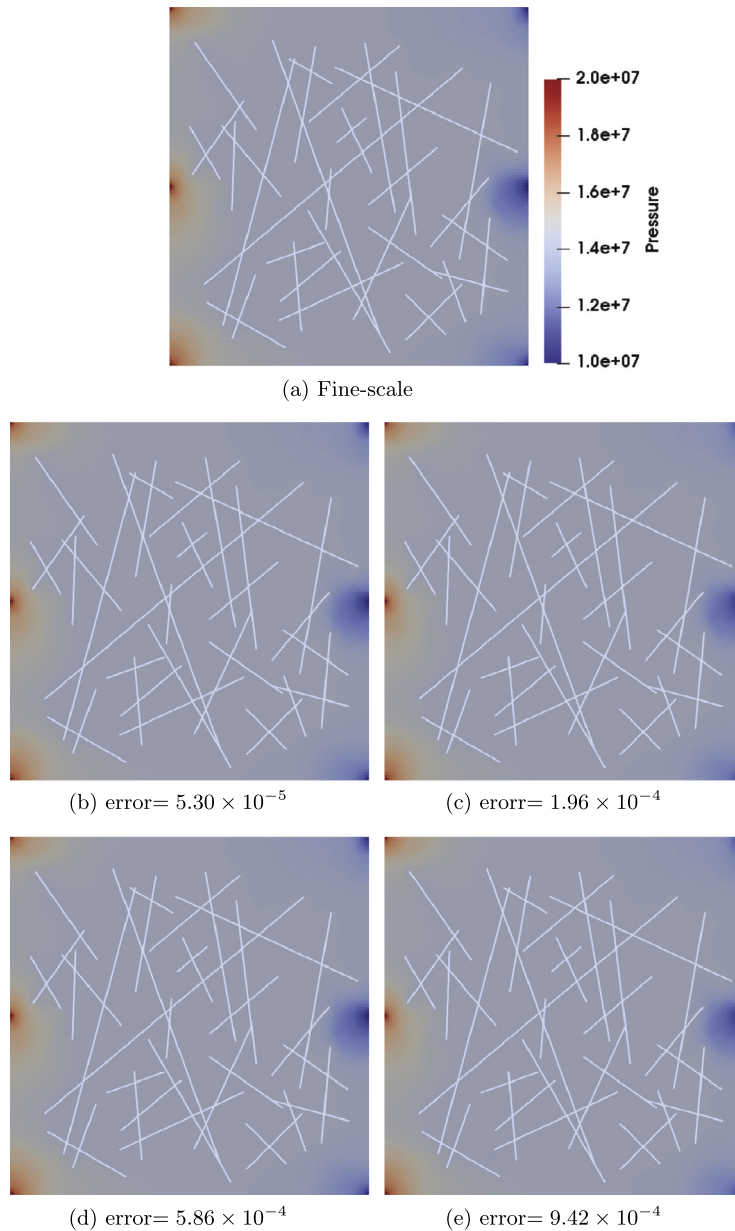(d) error= 5.86×10^{-4}　　　　　　　(e) error= 9.42×10^{-4}

Fig. 16. Pressure plots of 2D F-ADM test case (heterogeneous). Shown are fine-scale (a) and F-ADM results with thresholds of $\Delta S = 0.1$ (b), 0.3 (c), 0.5 (d) and 0.8 (e), respectively.

near the wells are kept at fine-scale resolution that is 8.73 percent out of 10.51 percent of active grid cells at the first time step. An increase in threshold correlates with a decrease in size of the F-ADM system as less active grid cells are used.

5. Conclusions

An algebraic dynamic multilevel method for fully-implicit simulations of multiphase flow in porous media with embedded discrete fractures, namely F-ADM, is presented in this work. Built on the embedded discrete fracture model (EDFM), the fine-scale fully implicit system was mapped into a multilevel dynamic grid, defined independently for matrix and fractures. This was achieved by development of the sequences of prolongation (local basis functions) operators for fractured media. These local multilevel basis functions were introduced after selection of the coarse nodes on both matrix and fracture sub-domains, with flexible matrix-fracture coupling. The front-detection strategy is used to employ fine-scale grids only where
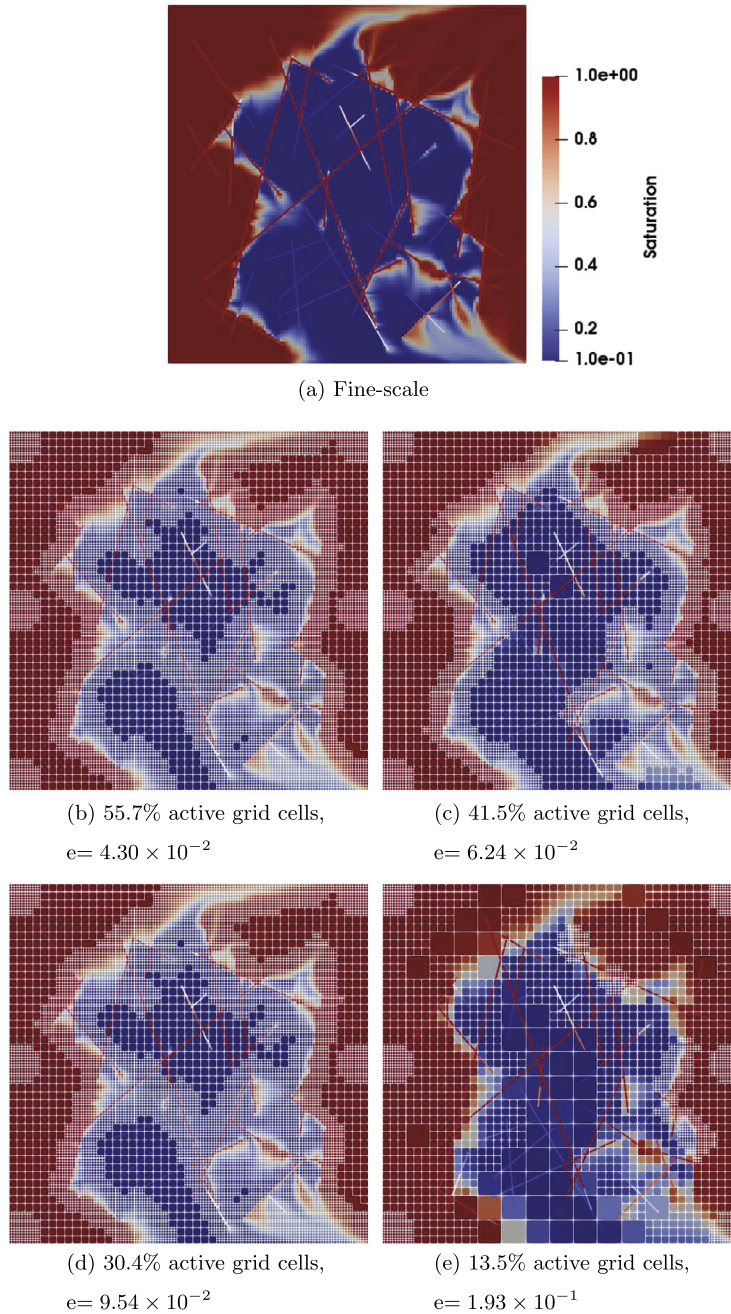
(a) Fine-scale

(b) 55.7% active grid cells,

e= 4.30×10^{-2}

(c) 41.5% active grid cells,

e= 6.24×10^{-2}

(d) 30.4% active grid cells,

e= 9.54×10^{-2}

(e) 13.5% active grid cells,

e= 1.93×10^{-1}

Fig. 17. Saturation distribution of 2D F-ADM test case (heterogeneous). Shown are fine-scale (a) and F-ADM solutions for thresholds $\Delta S = 0.1$ (b), 0.3 (c), 0.5 (d) and 0.8 (e), respectively.

needed, while multilevel multiscale grid is used elsewhere. The use of multiscale basis functions guarantees the accuracy of the global (pressure) unknowns where coarse grids are imposed.

Numerical results for both 2D and 3D test cases were presented to validate the EDFM fully-implicit implementation and investigate its accuracy. Then, the sensitivity of F-ADM to the type of pressure interpolator (i.e., with and without matrix-fracture coupling) and the fraction of active grid cells chosen indirectly by different threshold values was studied. The single-phase flow results show that the proposed multilevel interpolation strategy for embedded discrete fracture systems is accurate compared to the original 1-level multiscale finite-volume method. Multiphase flow results, with different amount of active dynamic grids, show that F-ADM is able to provide accurate results for flow in fractured media by employing only a fraction of the fine-scale grid-cells both in the rock matrix and in the fractures. It is expected that the greater the size of the domain, the lower the percentage of active grid cells compared to the global number of
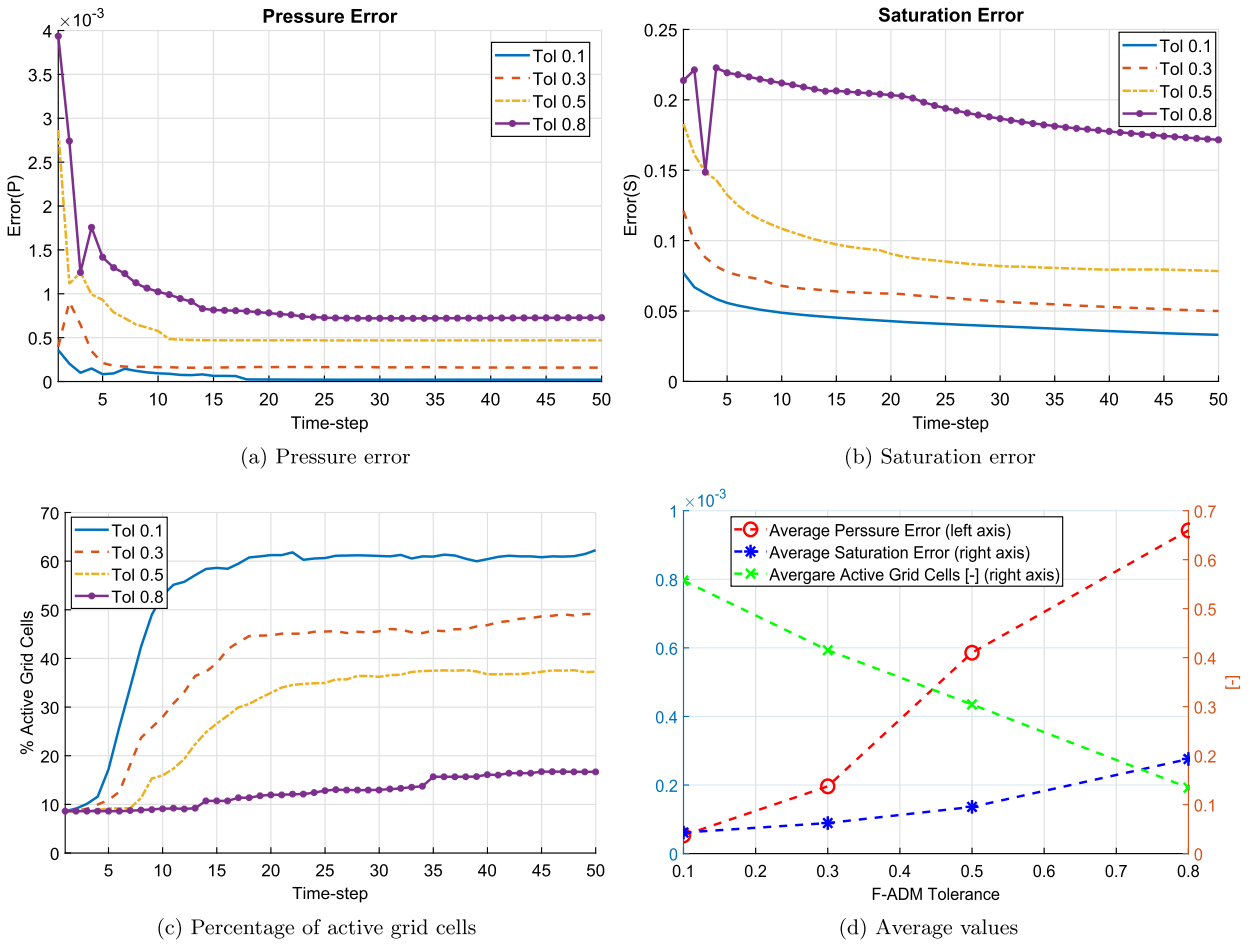
(a) Pressure error

(b) Saturation error

(c) Percentage of active grid cells

(d) Average values

Fig. 18. F-ADM error history for pressure (a) and saturation (b) calculated based on Eq. (25) during the simulation. The percentage of active grid cells (c) and the average errors over simulation time (d) are also presented.
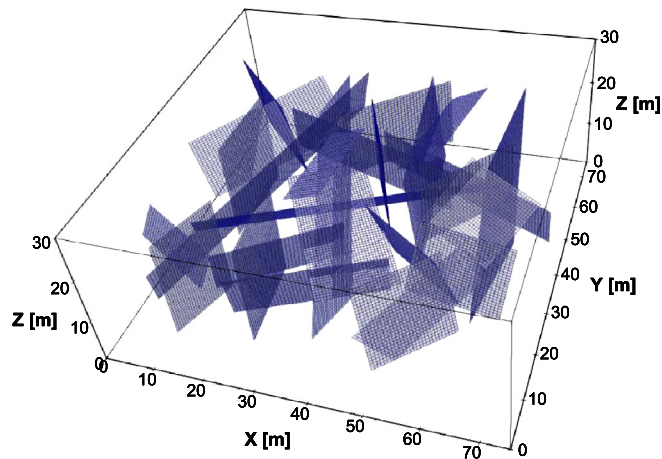

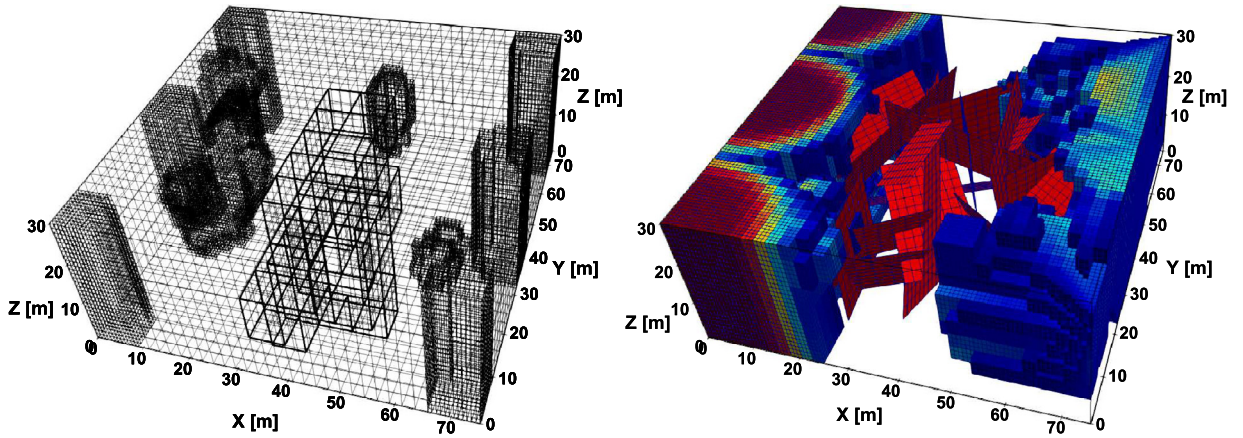**Fig. 19.** Test Case 6 – reservoir geometry and fracture network.

Fig. 20. Illustration of the F-ADM mesh at time-step 15 (left) and saturation distribution (right). Only saturation values higher than 0.5 are shown (right).
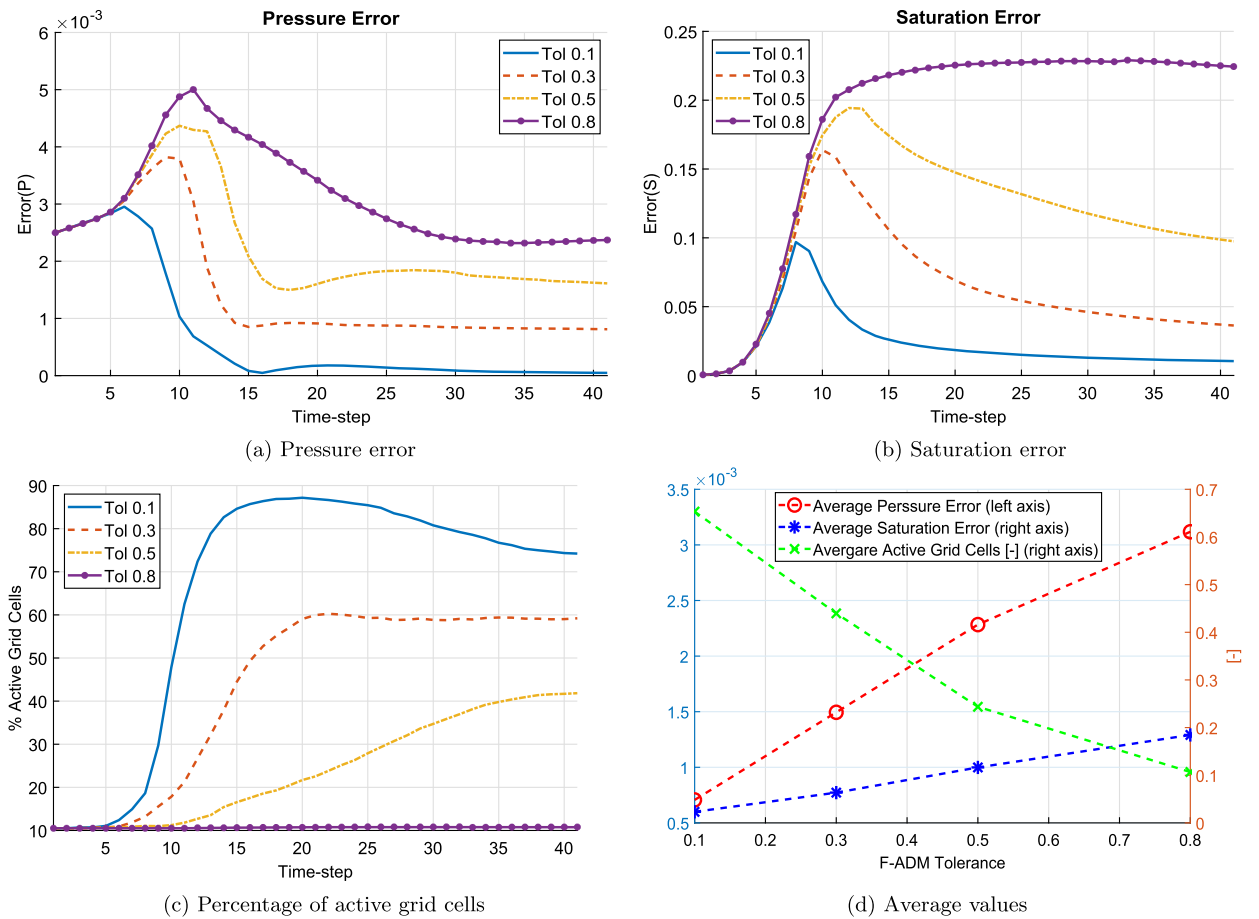

(a) Pressure error

(b) Saturation error

(c) Percentage of active grid cells

(d) Average values

Fig. 21. F-ADM error history for pressure (a) and saturation (b) calculated based on Eq. (25) during the simulation. The percentage of active grid cells (c) and the average errors over simulation time (d) are also presented.

fine-scale grids. As such, F-ADM casts a promising approach for simulation of multiphase flow in real-field fractured media.

Acknowledgements

References

[1] B. Berkowitz, Characterizing flow and transport in fractured geological media: a review, Adv. Water Resour. 25 (2002) 861–884.

[2] T.Y. Hou, X.-H. Wu, A multiscale finite element method for elliptic problems in composite materials and porous media, J. Comput. Phys. 134 (1997) 169–189.

[3] Y. Efendiev, T. Hou, T. Strinopoulos, Multiscale simulations of porous media flows in flow-based coordinate system, Comput. Geosci. 12 (3) (2008) 257–272.

[4] Y. Efendiev, S. Lee, G. Li, J. Yao, N. Zhang, Hierarchical multiscale modeling for flows in fractured media using generalized multiscale finite element method, GEM, Int. J. Geomath. 6 (2) (2015) 141–162, https://doi.org/10.1007/s13137-015-0075-7.

[5] P. Jenny, S.H. Lee, H.A. Tchelepi, Multi-scale finite-volume method for elliptic problems in subsurface flow simulation, J. Comput. Phys. 187 (2003) 47–67.

[6] P. Jenny, S.H. Lee, H.A. Tchelepi, Adaptive fully implicit multi-scale finite-volume method for multi-phase flow and transport in heterogeneous porous media, J. Comput. Phys. 217 (2006) 627–641.

[7] H. Hajibeygi, G. Bonfigli, M. Hesse, P. Jenny, Iterative multiscale finite-volume method, J. Comput. Phys. 227 (2008) 8604–8621.

[8] I. Lunati, S.H. Lee, An operator formulation of the multiscale finite-volume method with correction function, Multiscale Model. Simul. 8 (1) (2009) 96–109.

[9] Y. Wang, H. Hajibeygi, H.A. Tchelepi, Monotone multiscale finite volume method, Comput. Geosci. (2015) 1–16.

[10] O. Moyner, K.-A. Lie, A multiscale restriction-smoothed basis method for high contrast porous media represented on unstructured grids, J. Comput. Phys. 304 (2016) 46–71.

[11] M. Berger, J. Oliger, Adaptive mesh refinement for hyperbolic partial differential equations, J. Comput. Phys. 53 (1984) 484–512.

[12] D. Han, C. Yan, L. Peng, A more flexible approach of dynamic local grid refinement for reservoir modeling, in: SPE 16014, SPE Symposium on Reservoir Simulation, 1–4 February, San Antonio, Texas, USA, 1987.

[13] G. Schmidt, F. Jacobs, Adaptive local grid refinement and multi-grid in numerical reservoir simulation, J. Comput. Phys. 77 (1988) 140–165.

[14] W. Mulder, R.G. Meyling, Numerical simulation of two-phase flow using locally refined grids in three space dimensions, in: SPE 21230, in: SPE Adv. Technol. Ser., vol. 1, 1991, pp. 36–41.

[15] M. Biterge, T. Ertekin, Development and testing of a static/dynamic local grid-refinement technique, J. Pet. Technol. 44 (1992) 487–495.

[16] M. Edwards, M. Christie, Dynamically adaptive Godunov schemes with renormalization in reservoir simulation, in: SPE Symposium on Reservoir Simulation, 28 February–3 March, New Orleans, Louisiana, 1993, SPE paper 25268.

[17] M. Edwards, A higher-order Godunov scheme coupled with dynamical local grid refinement for flow in a porous medium, Comput. Methods Appl. Mech. Eng. 131 (1996) 287–308.

[18] Z. Heinemann, G. Gerken, G. von Hantelmann, Using local grid refinement in a multiple-application reservoir simulator, in: SPE Reservoir Simulation Symposium, 15–18 November, San Francisco, California, USA, 1983, SPE paper 12255.

[19] B. Faigle, R. Helmig, I. Aavatsmark, B. Flemisch, Efficient multiphysics modelling with adaptive grid refinement using a MPFA method, Comput. Geosci. 18 (2014) 625–636.

[20] M. Cusini, C. van Kruijsdijk, H. Hajibeygi, Algebraic dynamic multilevel (ADM) method for fully implicit simulations of multiphase flow in porous media, J. Comput. Phys. 314 (2016) 60–79.

[21] M. Cusini, B. Fryer, C. van Kruijsdijk, H. Hajibeygi, Algebraic dynamic multilevel method for compositional flow in heterogeneous porous media, J. Comput. Phys. 354 (2018) 593–612.

[22] P. Dietrich, R. Helmig, M. Sauter, H. Hotzl, J. Kongeter, G. Teutsch, Flow and Transport in Fractured Porous Media, Springer, 2005.

[23] M. Karimi-Fard, L. Durlofsky, K. Aziz, An efficient discrete-fracture model applicable for general-purpose reservoir simulators, SPE J. (2004) 227–236.

[24] R. Ahmed, M.G. Edwards, S. Lamine, B.A. Huisman, M. Pal, Control-volume distributed multi-point flux approximation coupled with a lower-dimensional fracture model, J. Comput. Phys. 284 (2015) 462–489.

[25] V. Reichenberger, H. Jakobs, P. Bastian, R. Helmig, A mixed-dimensional finite volume method for two-phase flow in fractured porous media, Adv. Water Resour. 29 (2006) 1020–1036.

[26] A. Moinfar, A. Varavei, K. Sepehrnoori, R.T. Johns, Development of an efficient embedded discrete fracture model for 3d compositional reservoir simulation in fractured reservoirs, SPE J. 19 (2014) 289–303.

[27] T. Sandve, I. Berre, J. Nordbotten, An efficient multi-point flux approximation method for discrete fracture–matrix simulations, J. Comput. Phys. 231 (2012) 3784–3800.

[28] T. Sandve, E. Keilegavlen, J. Nordbotten, Physics-based preconditioners for flow in fractured porous media, Water Resour. Res. 50 (2014) 1357–1373, https://doi.org/10.1002/2012WR013034.

[29] S. Geiger-Boschung, S. Matthäi, J. Niessner, R. Helmig, Black-oil simulations for three-component, three-phase flow in fractured porous media, SPE J. 14 (2) (2009) 338–354, https://doi.org/10.2118/107485-PA.

[30] A. Fumagalli, S. Zonca, L. Formaggia, Advances in computation of local problems for a flow-based upscaling in fractured reservoirs, Math. Comput. Simul. 137 (2017) 299–324, https://doi.org/10.1016/j.matcom.2017.01.007.

[31] A. Sakhaee-Pour, M. Wheeler, Effective flow properties for cells containing fractures of arbitrary geometry, SPE J. 21 (3) (2016) 965–980, https://doi.org/10.2118/167183-PA.

[32] A. Fumagalli, L. Pasquale, S. Zonca, S. Micheletti, An upscaling procedure for fractured reservoirs with embedded grids, Water Resour. Res. 52 (8) (2016) 6506–6525, https://doi.org/10.1002/2015WR017729.

[33] J. Natvig, B. Skaflestad, F. Bratvedt, K. Bratvedt, K.-A. Lie, V. Laptev, S. Khataniar, Multiscale mimetic solvers for efficient streamline simulation of fractured reservoirs, SPE J. 16 (4) (2011) 880–888, https://doi.org/10.2118/119132-PA.

[34] H. Hajibeygi, D. Karvounis, P. Jenny, A hierarchical fracture model for the iterative multiscale finite volume method, J. Comput. Phys. 230 (24) (2011) 8729–8743.

[35] T.H. Sandve, I. Berre, E. Keilegavlen, J.M. Nordbotten, Multiscale simulation of flow and heat transport in fractured geothermal reservoirs: inexact solvers and improved transport upscaling, in: Thirty-Eighth Workshop on Geothermal Reservoir Engineering, Stanford, California, USA, 2013.

[36] M. Tene, M.S. Al Kobaisi, H. Hajibeygi, Algebraic multiscale method for flow in heterogeneous porous media with embedded discrete fractures (F-AMS), J. Comput. Phys. 321 (2016) 819–845.

[37] S. Shah, O. Møyner, M. Tene, K.-A. Lie, H. Hajibeygi, The multiscale restriction smoothed basis method for fractured porous media (F-MSRSB), J. Comput. Phys. 318 (2016) 36–57.

[38] S. Bosma, H. Hajibeygi, M. Tene, H.A. Tchelepi, Multiscale finite volume method for discrete fracture modeling on unstructured grids (MS-DFM), J. Comput. Phys. 351 (2017) 145–164.
[39] S.H. Lee, C.L. Jensen, M.F. Lough, An efficient finite difference model for flow in a reservoir with multiple length-scale fractures, in: SPE Annual Technical Conference and Exhibition, 1999, https://doi.org/10.2118/56752-MS.
[40] S. Lee, M. Lough, C. Jensen, Hierarchical modeling of flow in naturally fractured formations with multiple length scales, Water Resour. Res. 37 (3) (2001) 443–455.
[41] L. Li, S.H. Lee, Efficient field-scale simulation of black oil in naturally fractured reservoir through discrete fracture networks and homogenized media, SPE Reserv. Eval. Eng. (2008) 750–758.
[42] A. Fumagalli, L. Pasquale, S. Zonca, S. Micheletti, An upscaling procedure for fractured reservoirs with embedded grids, Water Resour. Res. 52 (8) (2016) 6506–6525.
[43] A. Fumagalli, S. Zonca, L. Formaggia, Advances in computation of local problems for a flow-based upscaling in fractured reservoirs, Math. Comput. Simul. 137 (2017) 299–324.
[44] J.H. Norbeck, M.W. McClure, J.W. Lo, R.N. Horne, An embedded fracture modeling framework for simulation of hydraulic fracturing and shear stimulation, Comput. Geosci. 20 (1) (2016) 1–18.
[45] S. Pluimers, Hierarchical Fracture Modeling Approach, Master's thesis, TU Delft, Department of Geoscience and Engineering, 2015.
[46] M. Tene, S.B. Bosma, M.S. Al Kobaisi, H. Hajibeygi, Projection-based embedded discrete fracture model (PEDFM), Adv. Water Resour. 105 (2017) 205–216.
[47] B. Flemisch, I. Berre, W. Boon, A. Fumagalli, N. Schwenck, A. Scotti, I. Stefansson, A. Tatomir, Benchmarks for single-phase flow in fractured porous media, Adv. Water Resour. 111 (2018) 239–258.
[48] D. van Batenburg, M. Bosch, P. Boerrigter, A. de Zwart, J. Vink, Application of dynamic gridding techniques to IOR/EOR-processes, in: SPE Reservoir Simulation Symposium, 21–23 February, The Woodlands, Texas, USA, 2011, 2011, pp. 1–16, https://doi.org/10.2118/141711-MS, SPE paper 141711.